

Article

# An Enhanced Approach for High-Strain Plasticity in Flat Anisotropic Specimens with Progressively Distorting Neck Sections

Giuseppe Mirone <sup>1,\*</sup>, Raffaele Barbagallo <sup>1</sup>, Giuseppe Bua <sup>1,2</sup>, Pietro Licignano <sup>3</sup> and Michele Maria Tedesco <sup>3</sup>

<sup>1</sup> Department of Civil Engineering and Architecture, University of Catania, Via Santa Sofia 64, 95123 Catania, Italy; raffaele.barbagallo@unict.it (R.B.); giuseppe.bua@phd.unict.it (G.B.)

<sup>2</sup> Department of Electrical, Electronic and Computer Engineering, University of Catania, Via Santa Sofia 64, 95123 Catania, Italy

<sup>3</sup> C.R.F. S.C.p.A, Metals, Corso Settembrini 40, 10135 Turin, Italy; pietro.licignano@external.stellantis.com (P.L.); michelemaria.tedesco@crf.it (M.M.T.)

\* Correspondence: giuseppe.mirone@unict.it

**Abstract:** Characterizing the behavior of ductile metals at high strains is essential in various fields. In the case of thin sheets, rectangular cross-section specimens are used to characterize these materials, typically by tensile tests. Unlike cylindrical specimens, flat ones pose additional challenges for the hardening characterization at high strains, especially in the post-necking phase, which, for many high-strength steels, may cover most of the plastic strain range. After the onset of global necking, the rectangular cross-sections tend to distort with respect to their original shape, as their edges progressively curve and bulge inward. The localized necking occurring after the global one in thinner specimens, further distorts the necked zone. Additionally, sheet metals usually exhibit anisotropic characteristics that affect the derivation of the stress–strain curve and need to be dealt with. No exact method exists for the stress–strain characterization of ductile thin sheets at high strains from tensile tests. Although several approximate methods are available in the literature, they either discard the post-necking range or require highly advanced and complex experimental setups not suitable for industrial applications (e.g., 3D DIC). Then, this work proposes a relatively simple methodology for the experimental characterization of anisotropic thin sheet metals through tensile tests on rectangular cross-section specimens that delivers the true stress–strain curve of the material, extended over the necking range and up to fracture, accurately assessing the anisotropy and the distortion of the neck section. The proposed methodology, employing a standard single-camera experimental setup, is illustrated here, referring to four different steels for automotive applications with reference to a single material orientation; it is intended as representative of the repeated procedure involving tensile tests along 3 or more material directions in order to describe the whole anisotropic plastic response. A detailed comparison between the novel methodology and four other common approaches is carried out, highlighting the differences and the enhanced capabilities of the novel one proposed.

**Keywords:** sheet metals; true curves; necking; anisotropy; Lankford



**Citation:** Mirone, G.; Barbagallo, R.; Bua, G.; Licignano, P.; Tedesco, M.M. An Enhanced Approach for High-Strain Plasticity in Flat Anisotropic Specimens with Progressively Distorting Neck Sections. *Metals* **2024**, *14*, 578. <https://doi.org/10.3390/met14050578>

Academic Editors: Maciej Motyka and Carlos Garcia-Mateo

Received: 1 March 2024

Revised: 2 May 2024

Accepted: 9 May 2024

Published: 14 May 2024



**Copyright:** © 2024 by the authors. Licensee MDPI, Basel, Switzerland. This article is an open access article distributed under the terms and conditions of the Creative Commons Attribution (CC BY) license (<https://creativecommons.org/licenses/by/4.0/>).

## 1. Introduction

The remarkable mechanical properties of modern advanced sheet metals, such as high resistance, ductility, formability, and lightness, make these materials very attractive for several engineering applications. The technological processes involved in the production of sheet metals can strongly affect their mechanical response, often inducing anisotropic characteristics.

An accurate derivation of the tensile true stress–true strain curve is a necessary step for the extraction of the material’s hardening curve. Since ductile metals can have an extended post-necking straining history (e.g., up to 90% of the material’s life), the common engineering approaches based on the load vs specimen’s elongation data [1–4] are highly inadequate

to investigate the whole material's tensile behavior. Although the post-necking phases of material life are frequently underrated, they are crucial in the design of many structural applications requiring severe safety assessments under exceptional critical loadings, such as in the nuclear, automotive, aerospace, and ballistic fields.

The more advanced methodologies aiming at the derivation of true curves of sheet specimens include the acquisition of the local shrinking of the specimen's cross-section (reduction in width and thickness for flat geometries or reduction in diameter for cylindrical ones) by means of techniques such as digital image correlation (DIC) or optical extensometer (pixel count) [5]. In the work of Nguyen et al. [6], the true stress–strain curve was derived for two sheet alloys from full-field displacement measurements with a two-dimensional DIC method. However, as observed in Mirone et al. [7], the strain measurements on the specimen's surface can neglect the gradient of deformations through the thickness, underestimating or overestimating the true section-averaged strain. Sasso et al. [8] improved the 2D-DIC technique by associating it with Moiré phase-shift interferometry for the out-of-plane displacement measurements (orthogonal with respect to the specimen's surface) in order to reconstruct the complete three-dimensional deformed shape of a necked sheet specimen.

For tensile testing on sheet metals, the rectangular specimen's geometry is mandatory. The nominal gauge length/width ratio should be at least 5, in order to ensure a uniaxial stress state and uniform strains within the region between the specimen's shoulders. Moreover, a nominal width/thickness ratio between 1 and 2 is recommended to delay the inception of the localized necking phenomenon, which can drastically reduce the failure strain. Before the necking onset, the tensile true curve (and the corresponding material flow curve) can be simply determined from the experimental acquisition of load and gauge elongation. On the other hand, once the necking effects evolve during the test and the specimen assumes the so-called "hourglass-like" shape, the elongation-based approach misses the strain localization at the necking section, giving a very poorly accurate representation of the material behavior. If the material is isotropic or transversely isotropic, a single video acquisition is sufficient to determine the dimensions of the specimen's cross-section, either in flat or cylindrical geometry. In this latter case, if the specimen is anisotropic, the cross-section assumes an elliptical, deformed configuration, as observed in [9,10]. Also for sheet metals, the anisotropic behavior complicates the experimental measurements of local shrinking due to different modes of deformation along the transversal directions. By means of advanced techniques such as 3D Digital Image Correlation [11], it is possible to extend the tensile true stress curve in flat dog-bone specimens during the post-necking phase, but the imaging acquisition setup becomes more complex since at least two orthogonal cameras are required. Despite this, when a material is highly ductile, the localized necking phenomenon leads to the distortion of the rectangular cross-section, whereas its edges assume an increasing curvature towards the center, causing a reduction in the net resistant area with respect to the gross, rectangular one. Zhang et al. [12,13] conducted a numerical simulation campaign in order to establish a relationship between the reduction in the specimen's cross-section and its thinning during necking evolution.

The localization of plastic strains in the necking section forms the typical inclined bands, which, for isotropic materials, are oriented at 55 degrees with respect to the specimen axis. Cazacu and Rodríguez-Martínez [14] observed that this inclination strongly depends on the anisotropic behavior of sheet metals.

In this work, the authors recall and further develop the methodology discussed in a previous paper [7] for the determination of the true curve of anisotropic alloys from tensile tests on rectangular specimens by using a standard single camera experimental setup and fracture surface analyses. The proposed methodology has been adopted to investigate the tensile behavior of four different steels for automotive applications, comparing different degrees of approximation methods adopted for calculating the true stress and true strain, and highlighting the enhanced capabilities of the novel proposed one.

It is important to specify that the determined true curve is not the material's flow curve and is not exhaustive for describing the hardening, except for the pre-necking phase alone. At the same time, it is the most close and essential piece of information we have from experimental tests to derive the hardening curve. Indeed, many direct and indirect methods have been implemented by researchers in order to deplete the contribution of stress triaxiality from the true stress curve [15–20]. Whatever consideration is related to damage modeling and failure prediction of ductile metals cannot be performed unless a thorough description of the material's plasticity, extended up to large strains and failures, is available as a prerequisite. Moreover, the complete characterization of the plasticity of anisotropic sheets requires additional experimental tests along different directions and loading conditions (e.g., compression, torsion, shear) [21–23], together with a theoretical model to describe the material behavior (e.g., Hill [24,25], Cazacu [26,27], Barlat [28,29]).

## 2. Classical and Innovative Procedures for the Stress–Strain Characterization of Ductile Sheet Metals

Modern metal alloys try to combine high strength with high ductility in order to obtain structures as light as possible for the given nominal working loads capable of large deformations under exceptional loads in order to adsorb as much energy as possible before failure. High strength is known to anticipate the necking onset, while high ductility means high failure strains. Therefore, such materials will undergo pronounced necking conditions over most of their plastic straining life.

For round specimens, the necking phenomenon only affects the conversion of the true stress into an estimate of the flow stress. Instead, for flat and thin-sheet specimens, it also affects the whole derivation of the true stress and true strain from experiments. While the estimate of the post-necking flow curve starting from the experimental true curve has received great attention in the literature [12,13,15,16], the whole derivation of the experimental true curve after necking onset, which is the basis to derive any flow curve, has received less attention despite the fact that, in the case of flat specimens, it may present significant challenges.

Referring to the smooth specimen with rectangular cross-section shape and nomenclature shown in Figure 1, the true stress and the true strain are defined as the section-averaged axial stress and the section-averaged axial strain as shown in Equations (1) and (2), where  $F$  is the tensile load and  $A_0 = w_0 t_0$  and  $A = wt$  are, respectively, the specimen's cross-section in the initial undeformed configuration and in the current deformed state.

$$\varepsilon_{true} = \ln\left(\frac{A_0}{A}\right) \quad (1)$$

$$\sigma_{true} = \frac{F}{A} \quad (2)$$

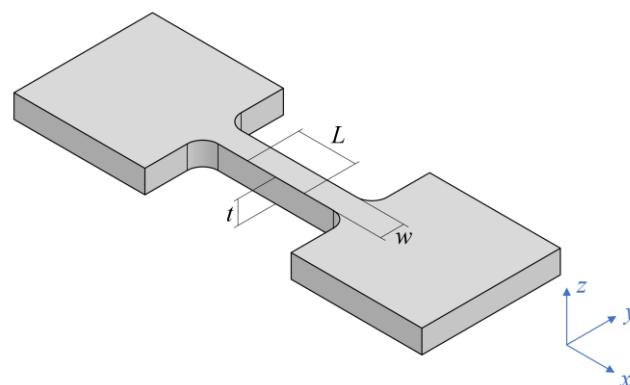


Figure 1. Specimen's relevant lengths and reference system.

For a smooth tensile specimen with a rectangular cross-section, as long as the volume of the gage length remains a straight parallelepiped, the true curve can be determined through five different experimental postprocessing approaches that, as explained below, are coincident with each other and are all nominally accurate only before necking onset and only for isotropic metals. Considering that many high-strength alloys exhibit early necking (e.g., at strains below 0.05) and late failure (e.g., at effective neck strains exceeding 0.5), it is evident that the choice between such methods cannot be arbitrary. Furthermore, the fact that most sheet metals are intrinsically anisotropic due to the rolling process, further restricts the possibility of arbitrarily selecting one stress–strain approach over another.

The five approaches used for the derivation of a true curve are reported below in order of increasing accuracy.

### 2.1. *L*-Based (Measurements of the Gage Length)

The most common method used for the determination of the true stress–strain curve is based on the measurement of the gage length elongation, called here *L*-based. With the hypothesis that the parallelepiped volume of the gage section remains constant, actually valid only before necking, it is possible to state that  $A = A_0 L_0 / L$ , being  $L_0$  and  $L$  the original and the current elongated gage length. This equation can be substituted into Equations (1) and (2), yielding the length-based definitions of strain and stress shown in Equations (3) and (4).

$$\varepsilon_{true-L} = \ln\left(\frac{L}{L_0}\right) \quad (3)$$

$$\sigma_{true-L} = \frac{F}{A_0} \cdot \frac{L}{L_0} \quad (4)$$

This approach is widely used since the elongation measurements are very easy to perform. However, the accuracy of the length-based stress–strain curve decays due to the diffused necking phenomenon as the specimen assumes the hourglass-like shape.

### 2.2. *DIC*-Peak (Local Peak Strain from Digital Image Correlation)

Another possible approach considers the local longitudinal peak strain read on the surface by the DIC instead of the *L*-based volume-averaged strain, assuming that the former is better than the latter at providing an estimate of the section-averaged plastic strain.

This approach may occasionally give quite accurate results, but it is formally wrong because, depending on the aspect ratio of the cross-section and on the hardening properties of the material at large strains, the peak of axial strain from DIC measurements on the necked specimen can be either larger or smaller than the neck-averaged axial strain. As a general indication, thin cross-sections make the DIC peak higher than the effective area-based true strain, while thicker cross-sections make it lower than the area-based true strain (Figure 2). It certainly exists an aspect ratio  $t/w$  that, for each material, delivers the DIC peak very close to the effective true strain, but its identification requires knowledge of the material hardening, which is the target of the whole investigation for which the strain is necessary.

Within the accuracy limits of assuming that the *DIC*-peak strain is representative of  $\varepsilon_{true}$ , the true stress and strain can be obtained as in Equations (5) and (6), where  $A = A_0 \cdot e^{\varepsilon_{true-DIC}}$  delivers the current deformed cross-section of the specimen.

$$\varepsilon_{true-DIC} \approx \varepsilon_{DIC-Peak} \quad (5)$$

$$\sigma_{true-DIC} \approx \frac{F}{A_0} \cdot e^{-\varepsilon_{true-DIC}} \quad (6)$$

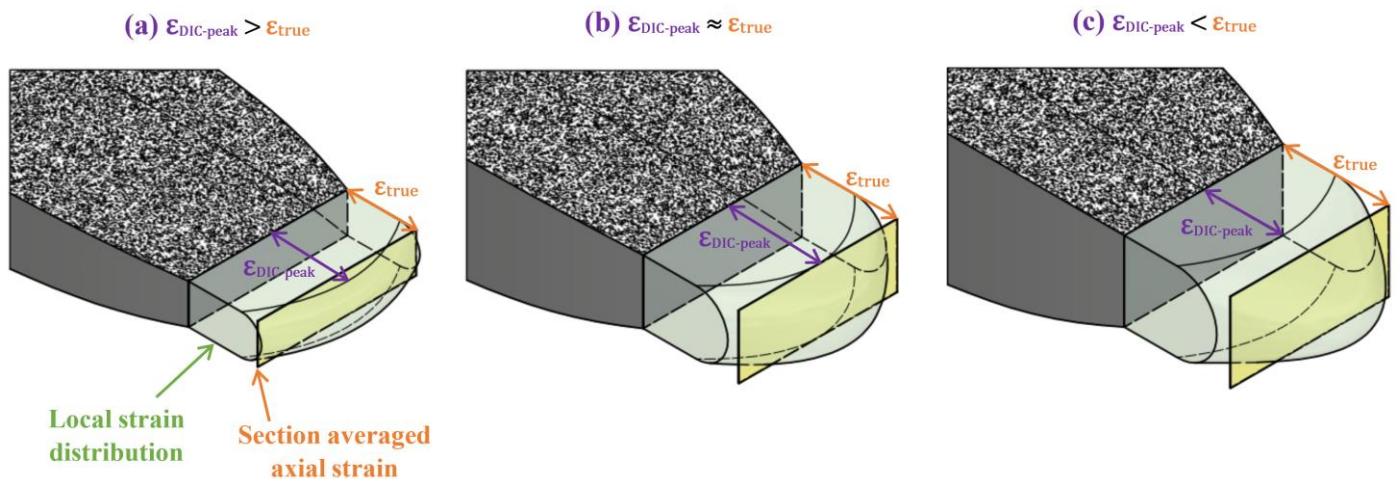


**Figure 2.** Difference between DIC peak local strain and section averaged axial strain depending on the effective local strain distribution due to the specimen's shape.

### 2.3. $w$ -Based (Measurements of the Neck Width)

If the material is isotropic and assuming that the specimen's cross-section is not affected by any distortion effect, then the "thinning ratio"  $t/t_0$  remains approximately equal to the "shrinking ratio"  $w/w_0$  during the entire post-necking phase of the tensile response. As a consequence of this observation, for isotropic material, from the experimental measurement of the width  $w$ , the thickness  $t$  is derived as  $t = (t_0/w_0) \cdot w$ . Therefore, the cross-section can be expressed as  $A = t \cdot w = (t_0/w_0) \cdot w^2$  and Equations (1) and (2) become Equations (7) and (8).

$$\epsilon_{true-w} \approx 2 \cdot \ln\left(\frac{w_0}{w}\right) \quad (7)$$

$$\sigma_{true-w} \approx \frac{F}{\frac{t_0}{w_0} \cdot w^2} \quad (8)$$

This method, called here  $w$ -based, is an improvement of the  $L$ -based one because, for isotropic materials, it extends the true curve beyond the necking onset and up to failure, provided that the neck section remains rectangular up to incipient failure. Unfortunately, this condition is not always true, as for some materials/specimens, the neck section progressively distorts and assumes the shape of a quadrilateral with inward-curved edges, inscribed within the nominally rectangular neck.

It is worth noting that, when the material is rather anisotropic, the accuracy loss of the  $w$ -based curve all over the test is much less pronounced than the underestimation/missing data of the  $L$ -based curve after necking onset.

### 2.4. Anisotropy $L$ & $W$ -Based (Measurements of Length and Neck Width)

If the material response is anisotropic, then the constancy of the ratio  $t/w = t_0/w_0$  is not preserved during the test, and the thickness may either reduce at a lower or greater rate than the specimen width does (Figure 3 left and right, respectively).

Therefore,  $t$  cannot be derived from simple width measurements, and the above  $w$ -based approach is not accurate, before and after necking onset. Under such circumstances, the  $L$ -based procedure still applies only to the pre-necking range (as far as the conservation of the parallelepiped volume of the specimen still applies), but, to the best of the authors' knowledge, no better formulation of the true curve is available after necking onset. Then, a new procedure was proposed in [7] for deriving a true curve extended after necking onset of anisotropic tensile specimens. Combining the measurements of both  $L$  and  $w$ , the

thinning ratio  $t/t_0$  can be derived all over the pre-necking strain range thanks to the volume conservation of a straight parallelepiped specimen volume, according to Equation (9).

$$\frac{t}{t_0} = \frac{L_0 \cdot w_0}{L \cdot w} \quad (9)$$

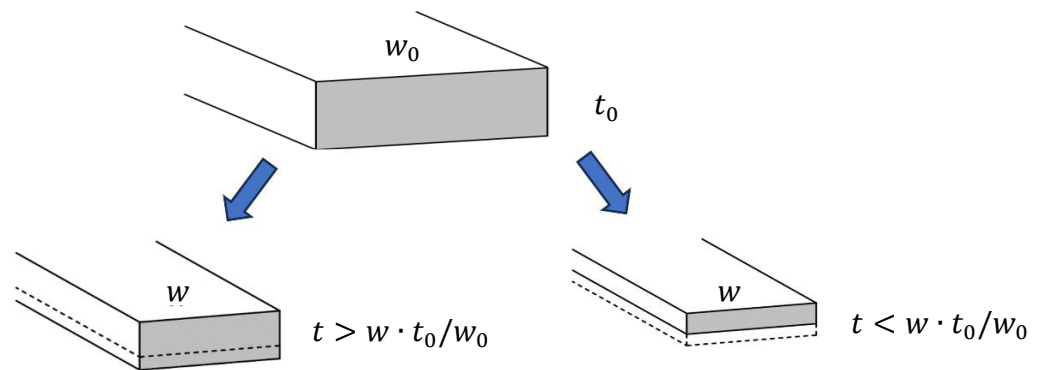


**Figure 3.** Anisotropic straining of cross-sections: thinning rate smaller (left side) or greater (right side) than isotropic shrinking ratio.

After necking onset, the specimen quits being a straight parallelepiped. Therefore, Equation (9) does not apply anymore, and its second member quits delivering any meaningful information about the thinning ratio.

For isotropic materials  $t/t_0 = w/w_0$  applies and the thinning versus shrinking trend is a straight 45-degree line. However, for anisotropic materials, the general unknown relationship between the thinning ratio  $t/t_0$  and the shrinking ratio  $w/w_0$  must be derived from pre-necking experimental measurements by relating the outcome of Equation (9) to the measured evolving ratio  $w/w_0$ . As better detailed in [7], before necking onset, the thinning ratio was found to follow very closely a power law of the shrinking ratio according to Equation (10).

$$\frac{t}{t_0} = \left( \frac{w}{w_0} \right)^z \quad (10)$$

The best-fit exponent of the power law  $z$  in Equation (10) can be identified using the pre-necking experimental data. Moreover, it delivers the Lankford coefficient, as shown in Equation (11).

$$\varepsilon_t = \text{Ln} \left( \frac{t}{t_0} \right) = \text{Ln} \left[ \left( \frac{w}{w_0} \right)^z \right] = z \cdot \text{Ln} \left( \frac{w}{w_0} \right) = z \cdot \varepsilon_w \rightarrow R = \frac{\varepsilon_w}{\varepsilon_t} = \frac{1}{z} \quad (11)$$

The outcome of Equation (10), identified by fitting the experimental data before necking, can then be used to predict the thinning ratio in the post-necking phase and up to failure. Direct measurements of the thickness after necking onset, either available at failure by analysis of broken specimens and/or recorded during the test if side-view camera acquisition is available in addition to the front-view one, can be used to generate valid post-necking thinning data and then to improve fitting the post-necking trends of Equation (10), eventually including variabilities within its  $z$  exponent, a first new important added feature proposed here in respect to the methodology presented in [7].

The knowledge of the thickness from Equation (10) all over the test allows for calculating the “anisotropy-aware” resisting neck area in Equation (12).

$$A_{Aniso} = w \cdot t = w \cdot t_0 \cdot \left( \frac{w}{w_0} \right)^z = t_0 \cdot \frac{w^{z+1}}{w_0^z} \quad (12)$$

This neck section, accounting for independent shrinking/thinning rates due to anisotropy, can finally be introduced into the usual formulae for the area-based true stress (current load/area ratio) and true strain (logarithm of initial to current area ratio), so delivering the true curve *approximation #4 Aniso*, firstly proposed in [7] and updated in this work with the variability of  $z$ .

### 2.5. Distortion + Anisotropic (High-Strain Distortion of Anisotropically Shrinking Cross-Section)

This fifth characterization method is the second fundamental improvement proposed here with respect to the methodology presented in [7]. The true curve of the *approximation #4 Aniso* still includes an underlying hypothesis that, for some materials and specimen proportions, may be just approximate: it is the assumption that the neck section of the specimen remains rectangular until failure, although changing its proportions due to anisotropy, and its area can be calculated as the product of width by thickness  $A = t \cdot w$ .

Instead, depending on the aspect ratio of the cross-section of each specimen  $t_0/w_0$ , and on the ductility of each material, diffused and localized necking progressively cause more or less intense distortions of the cross-section, which then loses its rectangular aspect. The edges of the cross-section progressively bend inward, so that the cross-section also takes on its own hourglass-like shape, similarly to what happens to the whole specimen's flat surface (see Figure 4).

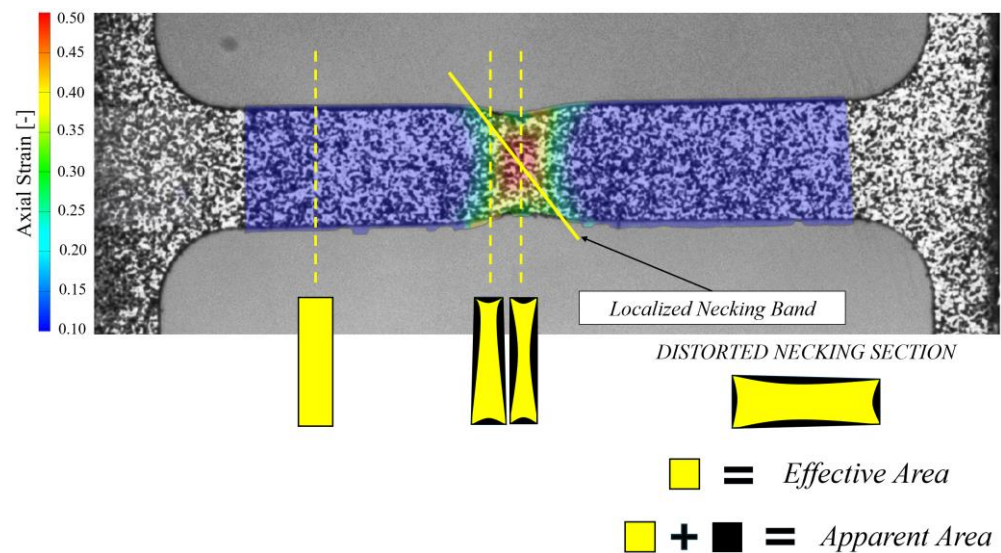


**Figure 4.** Scheme of the distorted neck section after localized necking takes place.

Then, the area of the effective resisting neck section becomes progressively smaller than the nominal rectangular one. As it will be shown in the next sections, the effective distorted resisting neck section  $A_{Dist+Aniso}$  may substantially differ from the nominally rectangular one  $A_{Aniso}$  calculated as shown in the previous section, simply inferred by width and thickness values at failure. In order to assess the effect of such distortion over the material hardening, a distortion coefficient  $D$  quantifying the area reduction should be obtained from experiments, as shown in Equation (13).

$$D = \frac{A_{Dist+Aniso}}{A_{Aniso}} \quad (13)$$

Until the necking onset, the cross-section remains undistorted. On the other hand, the value of the distortion coefficient at failure  $D_f$  can be calculated from the areas of the fracture surface measured by image analysis of broken specimens. Then, the evolution of  $D$  between necking onset and failure is estimated here by a simple linear, quadratic, or generally  $d$ -order power law connecting such two starting–ending points as shown in Equation (14). A quadratic option has been chosen here, as it is the minimum polynomial

order ensuring the required distortion values at necking onset and failure, together with a smooth transition from the undistorted strain range to the distorted one at necking onset.

$$D = \begin{cases} 1 & \text{before necking onset} \\ 1 - (1 - D_f) \cdot \left( \frac{\varepsilon_{True} - \varepsilon_{neck}}{\varepsilon_{fail} - \varepsilon_{neck}} \right)^d & \text{after necking onset} \end{cases} \quad (14)$$

The above function is then used to calculate the net distorted cross-section area between necking and failure, as shown in Equation (15).

$$A_{dist} = A_{aniso} \cdot D \quad (15)$$

Using  $A_{dist}$  in Equations (1) and (2) finally leads to the enhanced *approximation #5 Dist + Aniso* of the true stresses–true strain curves, firstly proposed in this work. It is worth underlining that, while the approaches from #1 to #5 are all quite accurate at low strains, procedure #5 is crucial for achieving accurate true stress–true strain curves at high deformation levels, where the correct assessment of the plasticity is a crucial prerequisite for ductile damage modeling and failure prediction.

In Table 1, the five implemented methods are summarized in order to provide a clear comparison. In the next sections, these techniques are applied to tensile tests on different steels, and their comparison will deliver useful information about the anisotropic response of the tested metals.

**Table 1.** Summary of the methodologies.

n.	Methodology	Necessary Input	True Curve Identification
1	<i>L-based</i>	$F, L$	Correct pre-necking also with anisotropic materials, very inaccurate post-necking.
2	<i>DIC-Peak</i>	$F$ , local peak axial strain from DIC	Correct pre-necking also with anisotropic materials, unknown inaccuracy of the post-necking.
3	<i>w-based</i>	$F, w$	Slightly incorrect pre-necking and post-necking only in case of anisotropic materials.
4	<i>Anisotropic L&amp;W-based</i>	$F, L, w$ , fracture surface ratio	Correct pre-necking also with anisotropic materials, correct post-necking for undistorting cross-sections.
5	<i>Distortion + Anisotropic</i>	$F, L, w$ , fracture surface ratio and distortion	Correct pre-necking and post-necking also with anisotropic materials and distorted cross-sections.

### 3. Experiments and Data Acquisition

The experimental campaign conducted in this study consists of quasi-static tensile tests on smooth specimens made of four different automotive steels: two low-carbon ferritic mild steels, one cold-rolled (called here CR04) and one hot-rolled (called here HR12), and two high-strength steels, one martensitic (called here MTC1300T), and one FORTIFORM 1180 ferrite/bainite matrix steel subjected to quenching-partitioning treatment (called here FORTIFORM).

The CR04 is used for deep-drawn inner layers of doors and hoods; the MTC1300T for side-impact reinforcing bars in the doors; the HR12 for supporting brackets to attach small components to the chassis; the FORTIFORM for energy-dissipation components in crashes (side spars).

Their nominal mechanical properties, referred to as the rolling direction provided by the manufacturer, are summarized in Table 2, while their chemical compositions are shown in Table 3.

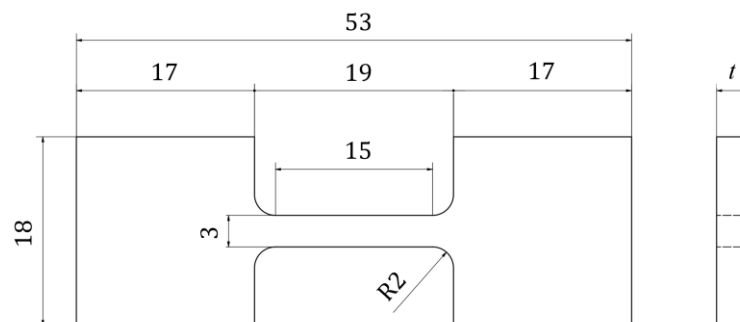
**Table 2.** Nominal mechanical properties of the tested materials provided by the manufacturer.

Grade	Yield Stress [MPa]	Ultimate Tensile Strength [MPa]	Elongation at Break [-]
CR04	161.9	294.9	46%
HR12	236.3	312.8	42%
MTC1300T	1059.6	1372.8	6.6%
FORTIFORM	912.1	1249.6	15.8%

**Table 3.** Chemical composition of the tested materials.

Mild Steels	C %max	Si %max	Mn %max	P %max	S %max	Ti %max	Cu %max	Al %min
CR04	0.08	0.5	0.5	0.025	0.02	0.3	0.25	0.01
HR12	0.1	0.5	0.5	0.025	0.03	0.3	0.25	0.01
High strength steels	C %max	Si %max	Mn %max	P %max	S %max	Ti+Nb %max	Cu %max	Al %min
MTC1300T	0.35	2.2	3	0.02	0.025	0.15	0.2	0.01
FORTIFORM	0.26	2.2	2.9	0.04	0.01	0.15	0.2	0.01

All specimens were waterjet-cut along the rolling direction from the above sheet metals, with the same in-plane geometry shown in Figure 5 and different thicknesses  $t$ , depending on the original sheet thickness (CR04 1.2 mm, HR12 3.5 mm, MTC1300T 1.3 mm, FORTIFORM 1.6 mm).

**Figure 5.** Specimens' geometry (dimensions in mm). Thickness  $t$  depends on the tested material.

The design of the specimens was first aimed at maintaining the initial width/thickness ratio  $w_0/t_0$  of the cross-section below 3 also for thinner sheets. In fact, thin cross-sections were found to lead to remarkably anticipated specimen failure and to a significant underestimation of the material ductility due to pronounced localized necking, which further limits the fracture strain and complicates the analysis of the material behavior [30]. Ideally, square cross-section specimens should also be pursued from thin sheets, whereas realistic flat specimens with a  $w/t$  ratio below 3 can also be cut from 1 mm thin sheets to already provide reasonable insight on the post-necking response of the material and greatly reduce the intensity of localized necking.

The uniform-section part of the specimen was designed 5 times longer than the width in order to ensure a good uniaxiality and to avoid disturbance of stress distributions due to the specimen's shoulders, even when necking and failure do not initiate exactly on the midsection of the specimen.

The quasi-static tests have been carried out at a nominal strain rate of  $3 \times 10^{-4} \text{ s}^{-1}$  using the experimental setup shown in Figure 6a. The employed hydraulic testing machine was an Instron 8872 (Instron, Norwood, MA, USA) with a 25 kN load cell. Throughout the tests, the specimens were monitored using two high-definition cameras positioned to

capture both frontal (Figure 6b) and lateral (Figure 6c) perspectives. Three repetitions have been made for each test.

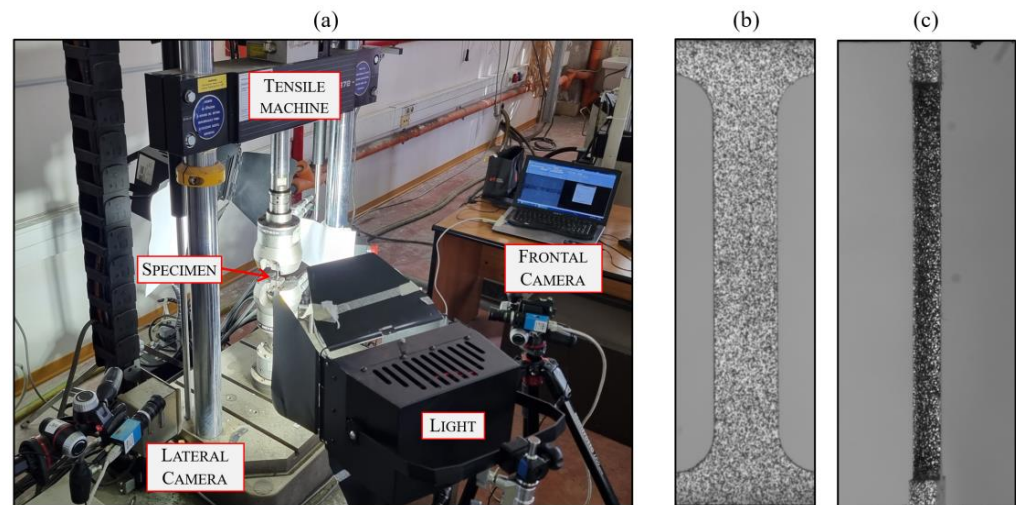


**Figure 6.** Experimental setup used for the tests (a) and examples of frontal (b) and lateral (c) acquired images of a specimen.

The DIC-Peak axial strain, the nominal 6 mm gage length  $L$  centered on the neck section, and the neck width  $w$  of all the tests were evaluated from DIC analysis and pixel count on images of the front-view video. The side-view video was used only with pixel count without DIC for double-checking the thickness predictions obtained with the procedure proposed in [7] and further updated here, as it will be discussed ahead. The resolution of the acquired images ensured that the minimum width at failure was covered by nearly 120 pixels, so a worst-case uncertainty of 2–3 pixels introduced a measurement error of  $w_f$  below 3%. The side-view acquisitions of thickness measurements delivered a minimum of 20 pixels at failure for the CR04 steel, which was the most ductile material tested undergoing huge thickness reduction at failure (twice or more of that number of pixels was found in the thickness of other “normally-thinning” materials, see Figure 7). However, the pronounced contrast due to no light reflections in the side view allows a near-sub-pixel estimate for the identification of the profile and a fairly acceptable minimum accuracy within 5% in the measurement of  $t_f$  at failure for the very pronounced thinning of the CR04 steel. Obviously, the measurement accuracy at the earlier necking stages of all tests (larger widths and thicknesses) is almost twice that at failure.

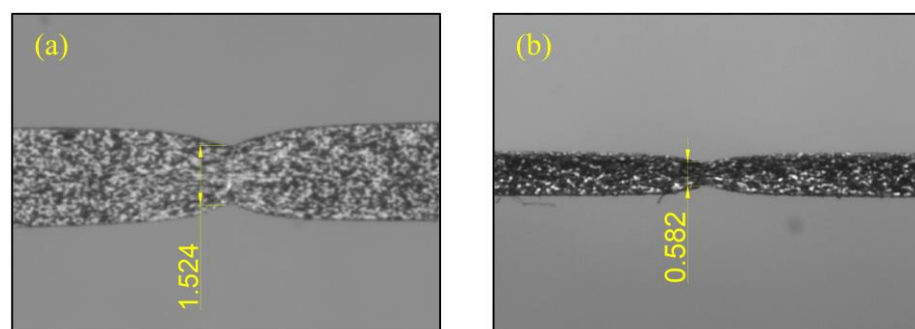


**Figure 7.** Image resolution for the measurement of the shrinking width from the frontal image (a) and thickness from the lateral one (b) for the tested most ductile material CR04.

The above data were used to derive the true curves #1 to #3 together with the shape-anisotropy assessments necessary to implement procedure #4 and to obtain the corresponding true curve. Instead, for assessing the neck distortion at failure and then deriving the true curve #5, the effective resisting area was measured by image analysis of the failed

specimens, as shown in Figure 8, representative of a failed specimen of each material, all scaled as indicated in the same figure. The gross rectangular section and its corresponding distorted counterpart are highlighted in yellow. The fracture surfaces are analyzed to determine the thickness/width ratio at fracture  $t_f/w_f$  and the distortion coefficient at fracture  $D_f$ , calculated as the ratio between the net distorted area at fracture  $A_{Aniso+Dist_f}$  and the gross quadrilateral area at fracture  $A_{Aniso_f}$ . This analysis solely focuses on these dimensionless ratios, without considering the absolute values of areas or lengths. The distorted section at failure was measured from the two halves of each test, for three repeated tests for each material series.

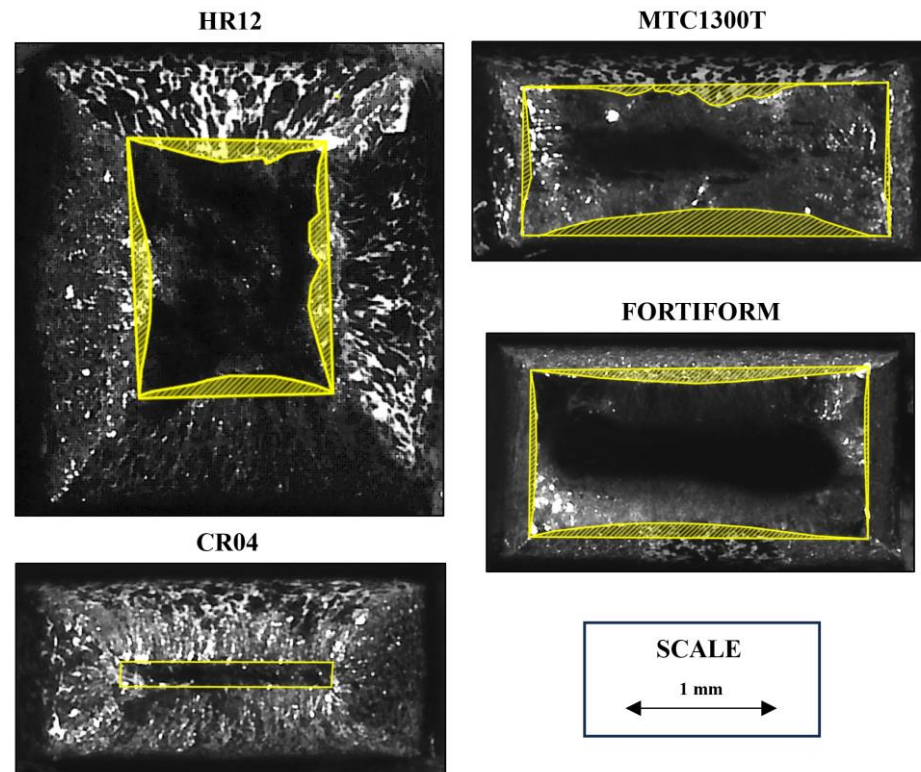


**Figure 8.** Examples of post-mortem photos of one fractured specimen per material with corresponding scale. The gross rectangular section and its corresponding distorted counterpart are highlighted in yellow.

#### 4. Application of the Stress–Strain Procedures to Different Metals

The experimental data discussed above were first used to assess the degree of anisotropy of the materials in terms of shrinking vs. thinning of the tensile specimens, according to the procedure proposed by the authors in [7].

In Figure 9, the normalized thinning ratio  $t/t_0$  calculated by Equation (9) is reported against the normalized shrinking one  $w/w_0$  (diamond-marks pre-neck and dotted line post-neck), directly measured from experiments. The beginning of the test corresponds to undeformed cross-sections ( $t_0/t_0 = w_0/w_0 = 1$ , upper-right point of each curve), and the plastic straining leads to progressively reducing cross-sections (the curves evolve backwards from the point of coordinates 1;1). The conservation of the parallelepiped volume expressed in Equation (9) is only valid in the pre-necking range. Then, these curves can only be considered physically meaningful from the test beginning up to the necking onset, roughly corresponding to the points where the experimental trends reach a minimum, as evidenced by the change from diamond dots to dashed lines.

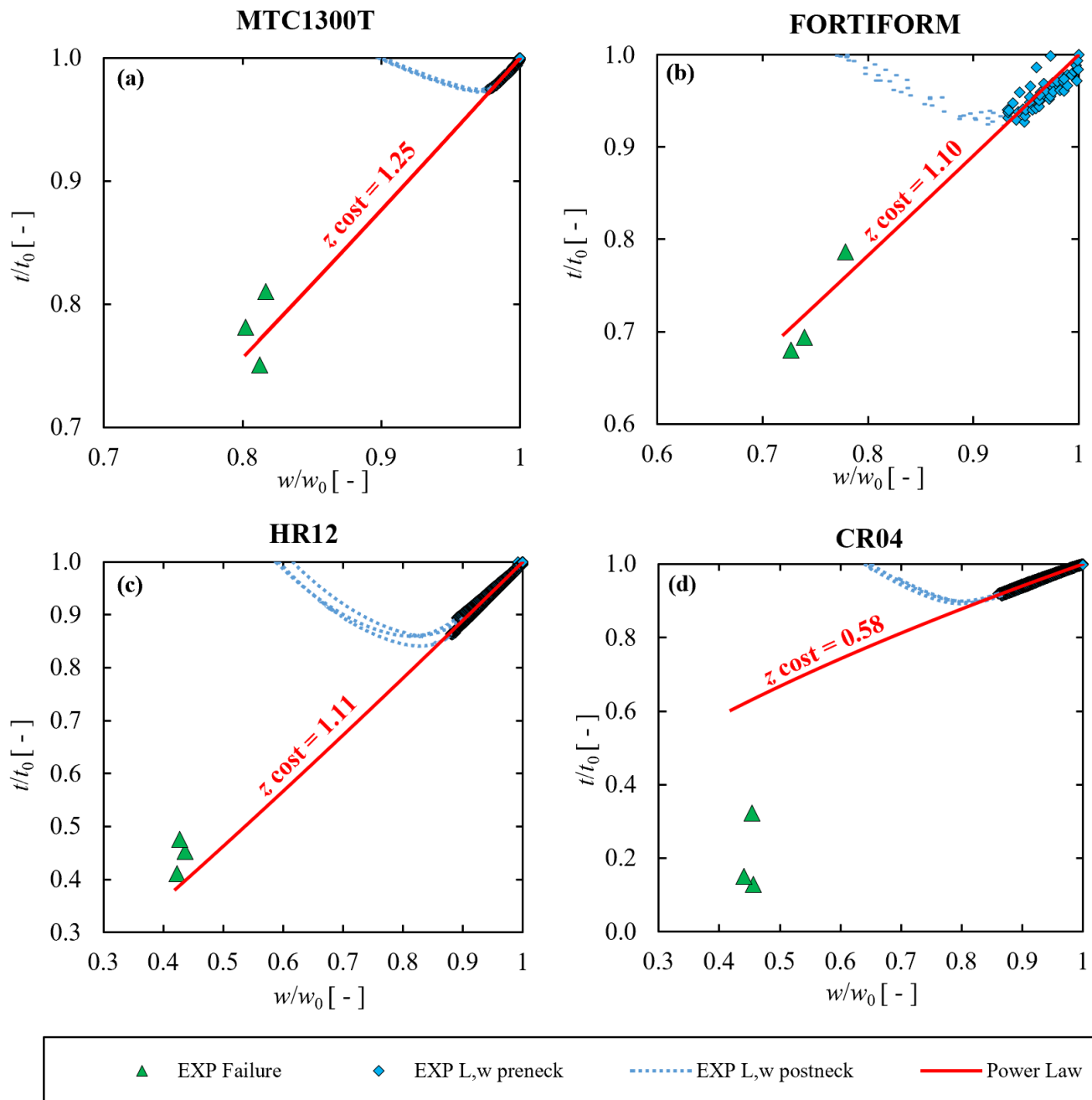


**Figure 9.** Values of  $t/t_0$  against  $w/w_0$  from the tests of MTC1300T (a), FORTIFORM (b), HR12 (c), and CR04 (d): values obtained from the experimental gauge length  $L$  and width  $w$  evaluated during the tests (light blue diamonds pre-neck and dotted line post-neck), values obtained from image analysis of fractured specimens (green triangles), and power law model with the constant exponent  $z$  calibrated for each material (red solid line).

The thinning and shrinking data at failure, calculated by measuring  $t_f/w_f$  from the images of fracture surfaces, are also reported in Figure 9 as isolated triangular points.

The power laws of Equation (10), with their best-fit exponents  $z$  determined from the pre-necking data of each test series, are reported in Figure 9 as continuous curves.

For three of the tested metals (Figure 9a–c), the constant value of  $z$  determined from pre-necking data and expressing the inverse of the Lankford coefficient also delivers reasonable predictions of thinning vs. shrinking until failure. Instead, for the CR04 mild steel, which exhibits a much greater thinning than all other metals, the power law of Equation (10) with the value of  $z$  determined before necking clearly misses to describe the trend of the

thinning after necking onset and up to failure. Then, for the CR04 steel, the variability of the exponent  $z$  of Equation (10) is proposed in this work to enhance the possibility of capturing the effective thinning–shrinking relationship after necking onset and up to failure.

The formula in Equation (16) delivers  $z$  remaining equal to the pre-necking best-fit value until necking onset. Then,  $z$  smoothly changes so that Equation (10) with the varying exponent complies with the experimental thinning and shrinking at failure, respectively  $t_f/t_0$  and  $w_f/w_0$ . The only free coefficient in Equation (16) is the exponent  $m$ , for calibrating, which the experimental evolution of the thickness in CR04 specimens has been measured from the images of the side-view camera.

$$\begin{cases} z = z_{neck} & \text{before necking} \\ z = z_{neck} + (z_{fail} - z_{neck}) * \left( \frac{\frac{w}{w_0} - \frac{w_{neck}}{w_0}}{\frac{w_{fail}}{w_0} - \frac{w_{neck}}{w_0}} \right)^m & \text{after necking} \end{cases} \quad (16)$$

Figure 10 shows that the power law of Equation (10) with the variable exponent of Equation (16) efficiently captures the evolving thinning vs. shrinking trend after necking onset, despite the remarkable trend changes.

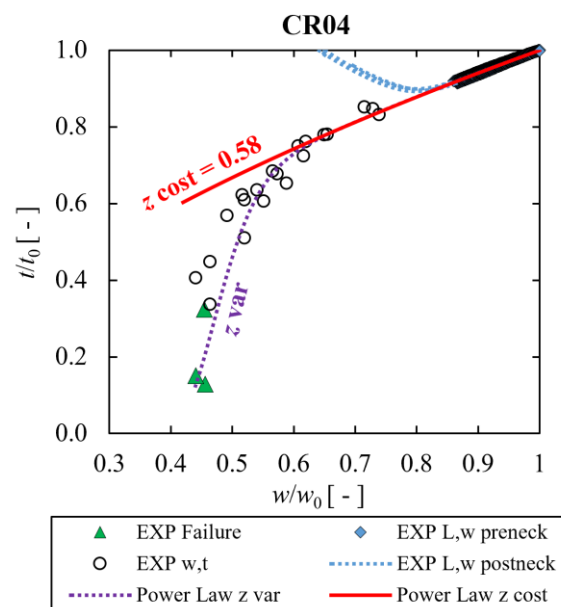


**Figure 10.** Values of  $t/t_0$  against  $w/w_0$  from the CR04 tests: values obtained from the experimental gauge length  $L$  and width  $w$  evaluated during the tests (light blue diamonds pre-neck and dotted line post-neck), values obtained from the experimental gauge thickness  $t$  and width  $w$  evaluated during the tests (white circles), values obtained from image analysis of fractured specimens (green triangles), power law model with the constant exponent  $z$  (red solid line), and power law model with the variable exponent  $z$  (purple dashed line).

It is worth underlining that before necking initiates, the stress state is uniaxial and compatible with the whole definition of the Lankford coefficient, which is then delivered by  $R = 1/z$ . After necking onset, the stress state becomes multiaxial, while the Lankford coefficient is defined under uniaxial stress conditions. Then, the exponent  $z$  still correctly expresses the relationship between thinning and shrinking, but its inverse  $R = 1/z$  might be the result of a mix between material anisotropy and the non-uniaxiality of the stress state; then, its physical meaning as a material parameter cannot be ensured anymore and might deserve further investigation.

As the evolution of the thinning–shrinking ratio has been identified, the evolving neck section  $A_{Aniso}$  is easily obtained, which accounts for the effective independent thinning and shrinking rates due to the material anisotropy.

The distortion ratio optically measured at failure also delivered the  $D$  function and, in turn, the  $A_{Dist+Aniso}$  estimate of the neck area, also including the effect of section edges curving inward at high strains. The relevant values for this assessment, averaged over three identical tests for each metal test series, are reported in Table 4.

**Table 4.** Relevant data for anisotropy and distortion assessment.

	CR04	HR12	MTC1300T	FORTIFORM
$w_f/w_0$	0.450	0.428	0.810	0.748
$t_f/t_0$	0.200	0.448	0.781	0.720
$z$ pre-neck	0.58	1.11	1.25	1.10
$R$ pre-neck	1.72	0.90	0.80	0.91
$m$	7.3	0	0	0
$D_f = \frac{A_{Dist+Aniso}}{A_{Aniso}} \Big _{fail}$	1	0.84	0.84	0.86

The evolving cross-sections, obtained according to procedures #1 (uniform straining, no-neck), #2 (DIC-Peak based on local data), #3 (isotropic neck), #4 (anisotropic neck), and #5 (anisotropic and distorting neck), finally delivered the corresponding five estimates of true curves for each material shown in Figure 11. The curves from all three tests are reported together for each approximation, also proving the good repeatability of the tests.

Before necking onset, all approaches are almost coincident with each other, including the #3  $w$ -based one, evidencing that the anisotropy just moderately affects the size of the resisting area at low plastic strains. After necking onset, the #1  $L$ -based true curves are the most underestimating ones, as they completely neglect the post-necking behavior, which, for ductile metals, covers most of the effective plastic strain range.

The true curves #2  $DIC$ -Peak account for anisotropy, but only at a local scale, and are either overestimating or underestimating the anisotropic cross-section depending on the specimen thickness. In fact, for the thicker specimens of the HR12 series, the  $DIC$ -Peak true curves lie much below the #4  $anisotropy$  curve, while for the thinner specimens, they lie above.

Procedure #3 can either overestimate or underestimate the cross-section, depending on whether the actual thinning of the anisotropic specimen is greater or smaller than that of the reference isotropic value.

True curves #4 and #5 are ordered in an increasing sequence because accounting for the distortion can only increase both stress and strain. However, the CR04 steel exhibits a very thin and, at the same time, very rectangular cross-section at failure, so the distortion in this series is negligible, and both approximations #4 and #5 for this material are actually coincident with each other.

Independently of the approximations in the experimental measurements, procedures #1 to #4 are also intrinsically approximate because, to different extents, they do not account for the necking, the anisotropy, and/or the distortion phenomena, certainly affecting the tensile tests. Instead, procedure #5, which is introduced for the first time in this work, accounts for all the above physical phenomena, and, therefore, the intrinsic approximation of the  $Distortion + Anisotropy$  true curves is just limited to the way the evolving anisotropic section reduction and its distortion are modeled (the eventual post-necking variability of  $z$  and/or of the distortion function  $D$ ). Then, procedure #5 true curve is the most accurate, and it will be taken as a reference in the following.

Figure 11 clearly shows that, depending on the material at hand, the validity of the  $L$ -based approach is limited to just the initial 10% to 30% of the effective material life (respectively for MTC1300T and CR04 steels). Afterwards, it completely fails to deliver any information about the hardening.

Depending on the relative thickness of the specimen, the  $DIC$ -Peak approach either overestimates or underestimates the reference true curve  $Distortion + Anisotropy$  according to the strain distribution in the cross-section. The  $w$ -based true curve can as well either

underestimate or overestimate the reference true curve, depending this time on the thinning rate being greater or smaller than the width reduction rate, i.e., Lankford coefficient  $R$  greater or lower than one. In particular, only CR04 steel exhibits a  $w$ -based true curve that is overestimated compared to the reference one. This demonstrates that it is the only material at hand exhibiting a Lankford coefficient  $R$  being greater than one (or an exponent  $z$  lower than one), as will be shown in the following. Considering all cases, the stress approximations at failure lie in the range between 10% (FORTIFORM steel) and 25% (MTC1300T steel).

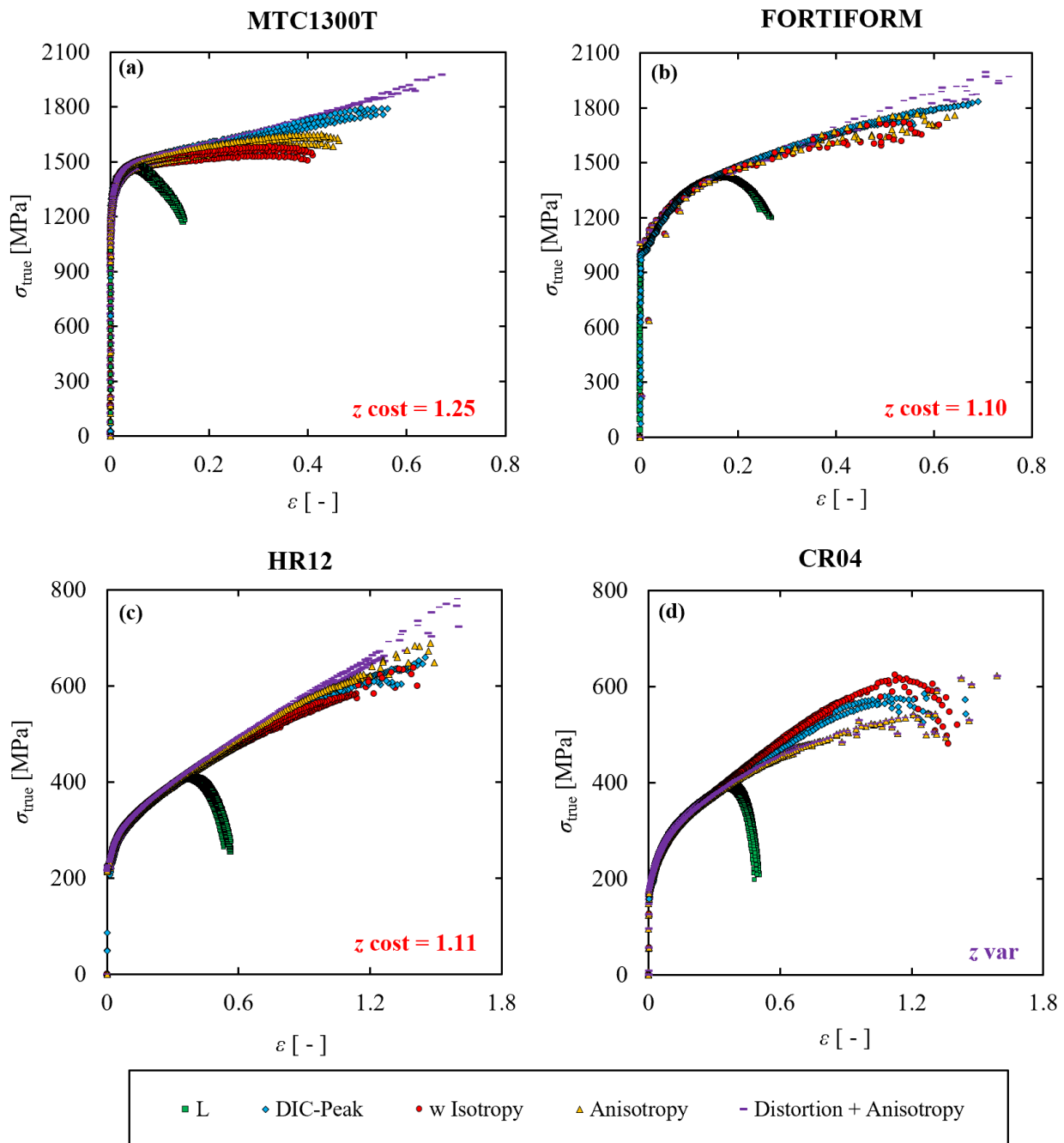


**Figure 11.** True stress–true strain curves obtained from the tests of MTC1300T (a), FORTIFORM (b), HR12 (c), and CR04 (d) with the different approaches: length-based (green squares), DIC-Peak based (light blue diamonds),  $w$ -based isotropic (red circles), Expo anisotropic (yellow triangles), and Expo anisotropic with section distortion (purple dashes).

The *anisotropy* approach, by neglecting the distortion effect, can only underestimate the reference true curve. *Distortion + anisotropy* were found, and the approximations ranged from 0 for the undistorted CR04 steel to a very substantial 45% in terms of strain at fracture and over 20% in terms of stress at fracture for the very distorted MTC1300T. This last piece of evidence shows the importance of the proposed methodology related to the distortion of the necking section first introduced in this work.

The true curves of the CR04 steel are the only ones in Figure 11 exhibiting an apparent softening trend at late test stages, while all other materials exhibit the expected monotonically increasing trends up to failure. This distinctive response of the CR04 steel is likely due to its great ductility and the slowly evolving fracture inside the cross-section, causing the neck section to continue progressively deforming between the onset of local fracture and the complete failure of neck section. While the initiated crack gradually spreads from the neck center toward the outer the neck section, the area calculated by outside visible features (width, thickness, and distortion) cannot reflect the effective resisting net area accounting for the spreading inner crack; this leads to underestimating the stress and delivers the apparent softening shown in Figure 11. In the other materials, fracture propagation within the neck is faster, and the shape of the completely fractured surface remains very close to that of the cross-section at the onset of the initial inner crack. Figure 8 confirms the different evolutions of the fracture surface of CR04 with respect to other materials.

The mean values and corresponding scattering ranges of strains at necking and at failure are reported in Figure 12 according to the different evaluation procedures. The CR04 and HR12 failure strains from the *DIC-Peak* methodology are reported but are compromised by premature DIC decorrelation in some of the tests. Given that before necking there is neither strain localization nor distortion, all the procedures except the *w-based* isotropic one must give the same necking strain estimates. Figure 12a shows very similar results with all the procedures, including the *w-based* isotropic one, for all the materials, evidencing once again that the anisotropy just moderately affects the size of the resisting area at low plastic strains.

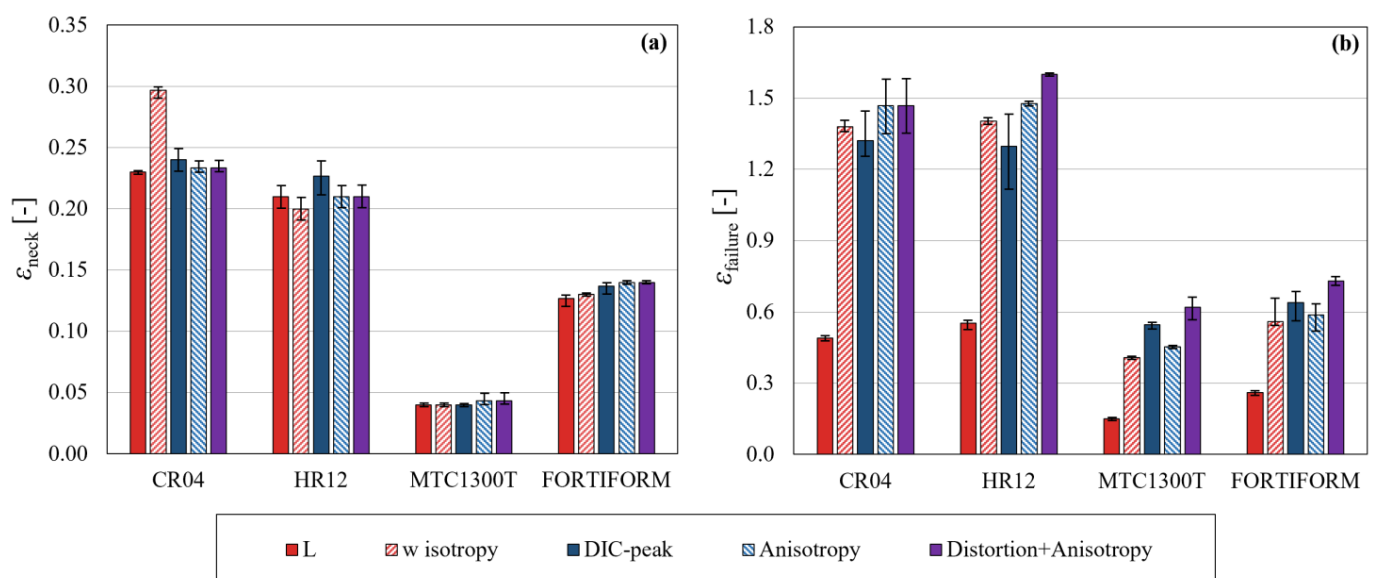


**Figure 12.** Mean values and corresponding scattering ranges of strains at necking (a) and at failure (b) obtained according to the different evaluation procedures discussed for the four analyzed materials.

On the other hand, considering again procedure #5 *distortion + anisotropy* as the reference one, the approximation of the *L-based* approach in the evaluation of the strain at failure is, respectively, 136% for the CR04, 179% for the HR12 steel, 320% for the MTC1300T steel, and 188% for the FORTIFORM steel (Figure 12b).

Finally, the different trends of the Lankford coefficient are compared in Figure 13, either calculated as the ratio of strains from  $L$  and  $w$  experimental values ( $L/w$ ), as the ratio of strains from DIC (*DIC-Peak*), or as the inverse of the exponent  $z$  related to procedure #4 (*Power Law*). The distortion affects the area regardless of the width–thickness directionality and then does not affect anisotropy-related features.

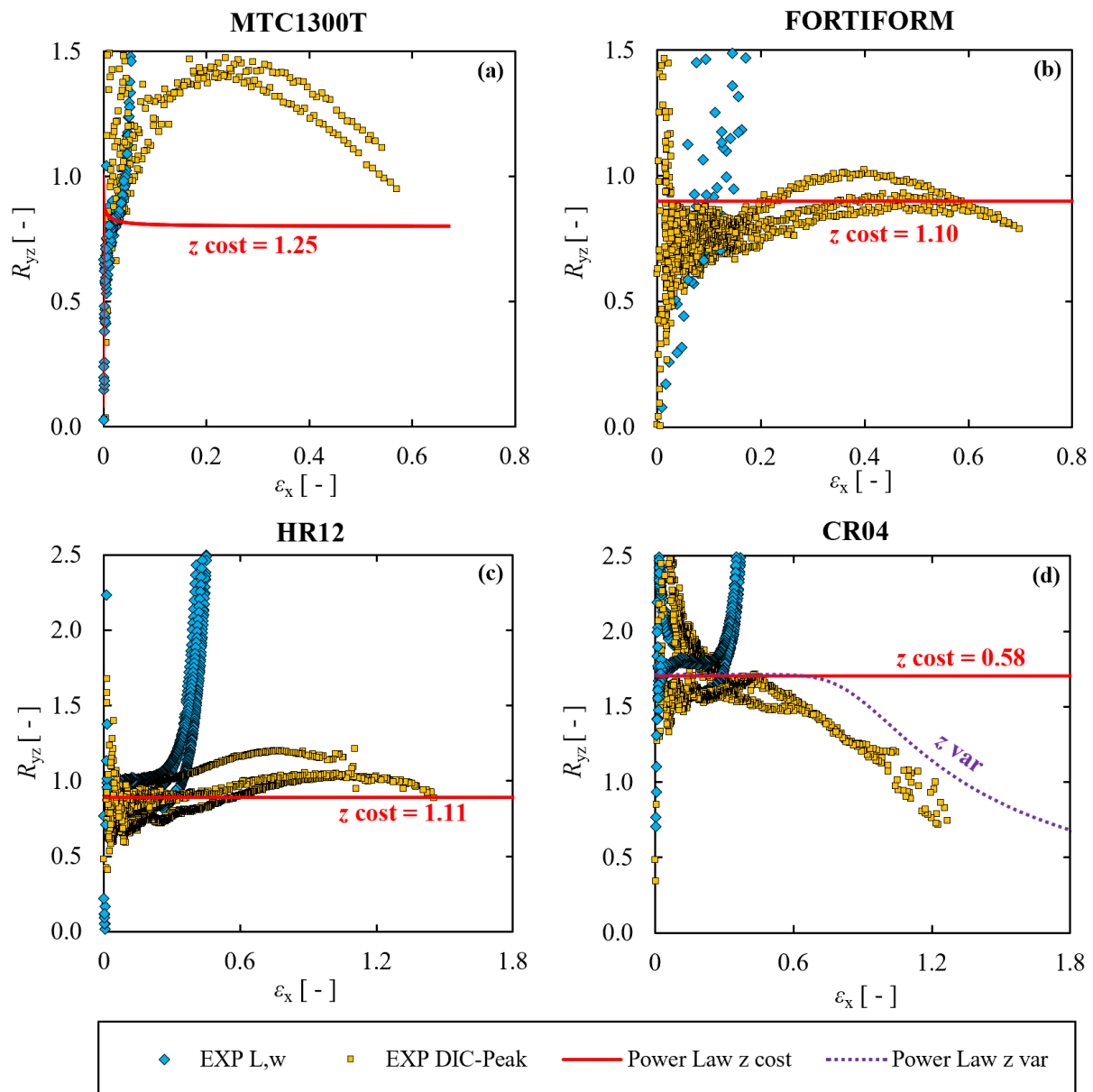


**Figure 13.** Lankford coefficient  $R$  versus axial strain obtained from the test series of MTC1300T (a), FORTIFORM (b), HR12 (c), and CR04 (d) with the different approaches: from experimental length and width (light blue diamonds), DIC-Peak based (yellow squares), power law model with the constant exponent  $z$  (red solid line), and power law model with the variable exponent  $z$  (purple dashed line).

As clearly visible in Figure 13, the *DIC-Peak* estimate of  $R$  is rather dispersed and oscillating because of the nature of local measurements, especially at low strains. It also reflects the high sensitivity to the choice of the local points of the specimen surface where data are acquired, sometimes forced by the deterioration of the speckle in the necked zone.

The section-averaged  $L, w$  estimate of  $R$  is simply derived from the volume conservation of the parallelepiped specimen before necking onset, as in Equation (17).

$$R = \frac{\varepsilon_w}{\varepsilon_t} = \frac{\text{Ln}\left(\frac{w}{w_0}\right)}{\text{Ln}\left(\frac{t}{t_0}\right)} \approx \frac{\text{Ln}\left(\frac{w}{w_0}\right)}{\text{Ln}\left(\frac{L}{L_0}\right) - \text{Ln}\left(\frac{w}{w_0}\right)} \quad (17)$$

Its trend is steadier and more repeatable than *DIC-Peak* data, although it too only applies before necking onset, as already discussed (see curve lines in Figures 9 and 10). Indeed, after necking onset,  $\text{Ln}(L/L_0)$  greatly underestimates the local axial strain, thus the denominator of Equation (17) underestimates  $\varepsilon_t$  and the whole Equation (17) overestimates  $R$ .

The *Power Law* estimate of the Lankford coefficient obtained as the inverse of the best-fit exponent  $z$  fitting the thinning vs. shrinking experimental trend before necking onset is instead a neat constant.

Both the  $z$  exponent delivering a fixed value of  $R$  and the outcome of Equation (17) are based on exactly the same experimental measurements, namely  $L$  and  $w$ , but the “raw” data in Figures 9 and 10 (width and thickness just normalized by their initial values) are much less dispersed than the same data just “refined” in Figure 13 after logarithms are extracted and their ratio is calculated for delivering the classical strain-based evaluation of  $R$ , which also tends to the undetermined form  $0/0$  at early plastic strains.

In general, all the derivations of the Lankford coefficient before necking onset always derive from the measurement of longitudinal and transverse displacements over the specimen surface, either between very close facets in the case of *DIC* local data or between finite-distance points for the  $L-w$  procedure. Then the  $L-w$  procedure for deriving  $R = 1/z$ , based on unprocessed thinning and shrinking, is just subjected to the approximations in the experimental measurements. Instead, the  $L-w$  data estimate of  $R$  according to Equation (17), includes the mathematical processing of the experimental measurements, which amplifies the error and the scattering. The *DIC-Peak* local approach also refines the experimental data by transforming displacements into strains and making their ratio, as in the in the previous case, other than calculating elongations on much smaller gage lengths, which, at early plastic stages, can deliver greater scattering already in the raw data.

In the case of early-necking materials (Figure 13a,b), the trend of  $R$  cannot even stabilize after the first yield before diverging; therefore, almost no information about the Lankford coefficient or the anisotropically shrinking cross-section is available by the *DIC-Peak* or the  $L-w$  strain-based procedures for these metals. In such cases, to derive the evolving cross-section accounting for its anisotropy, it is essential to rely on either thickness measurements from a second camera or at least thinning and shrinking values at failure measured on the fractured surface.

Looking at Figure 13, it is worth noting that only CR04 is characterized by a Lankford coefficient  $R$  greater than one (or exponent  $z$  lower than one). The fact that a material exhibits a Lankford coefficient greater or smaller than one depends on several factors, among which the most important are certainly the crystallographic structure and its orientation with respect to the principal directions of the specimen, as well as the thermo-mechanical treatments undergone by the material itself in the rolling process.

No details are available about the crystallographic structure; however, the materials subjected to high temperatures during their production, namely HR12 and FORTIFORM, are those with a Lankford coefficient closer to one, indicating nearly isotropic behavior, consistent with literature evidence [25]. On the other hand, the other two materials, CR04 and MTC1300T, exhibit Lankford coefficients, respectively, higher and lower than one.

Summarizing, as demonstrated in [7] for two metals and further confirmed here for four more metals, the trend of the thinning vs. shrinking ratio can be fit very efficiently by power functions whose exponent before necking delivers the Lankford coefficient and whose trend all over the test delivers the effective cross-section subjected to anisotropic deformation, evolving also in the post-necking range up to failure. The proposed proce-

dures improve the plastic characterization whenever the metal ductility is large enough to cause necking-induced strain localization (nonuniformity of cross-sections). For poorly ductile metals, tensile specimens almost preserve the uniformity of the cross-section along the gage length and their overall parallelepiped shape up to failure, so that the procedures at hand would just deliver duplicates of the length-based true curves.

## 5. Conclusions

In this work, the authors recalled and further developed the methodology discussed in a previous paper for the determination of the true curve of anisotropic alloys from tensile tests on rectangular specimens by using a standard single-camera experimental setup and fracture surface analysis.

In the pre-necking phase, measuring the gauge elongation and the width contraction, the specimen's thickness was derived by imposing the conservation of the parallelepiped specimen volume.

The resulting thinning parameter  $t/t_0$  was related to the shrinking  $w/w_0$  and their trend before necking was proved to follow very closely a power-law trend, whose exponent  $z$  is constant and was demonstrated to express the inverse of the Lankford coefficient.

The thinning and shrinking parameters at failure, measured by image analysis of the fracture surface, were found to be well aligned with the pre-necking trend identified by the power law for all materials except the CR04 steel. Then, as a first major improvement in respect to the previous work [7], a variable-exponent  $z$  was adopted in the power law for modeling the thinning vs. shrinking relationship after the necking onset of materials like the above metal; the actual anisotropy trend was obtained thanks to the optical measurements of the thickness from the analysis of the images from a second, side-view camera.

The power law model, with either a constant or variable exponent after necking onset, was shown to easily deliver the evolving cross-section of the specimen and, in turn, the true stress–true strain curve, accounting for anisotropic deformations up to failure.

A further important improvement in the procedure for deriving the true curve in respect to the previous work [7] was provided by assessing the amount of distortion in the fracture surface with respect to its nominal shape corresponding to thickness and width. This aspect allowed us to significantly improve the obtained true curve for very distorting section materials such as MTC1300T and FORTIFORM, with differences for MTC1300T up to 45% in terms of strain at fracture and over 20% in terms of stress at fracture.

In conclusion, the novel methodology proposed here was demonstrated to deliver the true stress–strain curves of the materials at hand extended up to fracture, accurately accounting for the anisotropy and the distortion of their cross-sections.

The proposed procedure delivers true curves with a higher-order accuracy and extended up to the effective failure strains based on simple experimental measurements, only requiring standard experimental equipment. These features make it suitable for the accurate characterization of anisotropic materials also in industrial environments.

Here the method is applied to specimens cut along a single material direction for demonstrative purposes, but the application of such a procedure to tests along three or more material orientations remains necessary to characterize the whole plasticity of anisotropic materials.

**Author Contributions:** G.M. formal analysis, investigation, methodology, writing, reviewing, supervision; R.B. formal analysis, investigation, methodology, writing, reviewing, validation; G.B. formal analysis, investigation, methodology, writing, reviewing, validation; P.L. formal analysis, investigation, methodology, writing, reviewing, funding acquisition; M.M.T. formal analysis, investigation, methodology, writing, reviewing, funding acquisition. All authors have read and agreed to the published version of the manuscript.

**Funding:** This work has been partially funded by European Union (NextGeneration EU), through the MUR-PNRR project SAMOTHRACE (ECS0000022).

**Data Availability Statement:** The raw data supporting the conclusions of this article will be made available by the authors on request.

**Conflicts of Interest:** The authors declare no conflicts of interest.

## References

1. Joun, M.; Eom, J.G.; Lee, M.C. A New Method for Acquiring True Stress–Strain Curves over a Large Range of Strains Using a Tensile Test and Finite Element Method. *Mech. Mater.* **2008**, *40*, 586–593. [[CrossRef](#)]
2. Zhao, K.; Wang, L.; Chang, Y.; Yan, J. Identification of Post-Necking Stress–Strain Curve for Sheet Metals by Inverse Method. *Mech. Mater.* **2016**, *92*, 107–118. [[CrossRef](#)]
3. Gao, Q.; Lu, C.; Li, H.; Li, J.; Han, J.; Chen, L. Anisotropy and Microstructural Evolutions of X70 Pipeline Steel during Tensile Deformation. *J. Mater. Res.* **2018**, *33*, 3512–3520. [[CrossRef](#)]
4. Tardif, N.; Kyriakides, S. Determination of Anisotropy and Material Hardening for Aluminum Sheet Metal. *Int. J. Solids Struct.* **2012**, *49*, 3496–3506. [[CrossRef](#)]
5. Zhu, F.; Lu, R.; Gu, J.; Tao, J.; Bai, P.; Lei, D. High-Resolution and High-Accuracy Optical Extensometer Based on a Reflective Imaging Technique. *Opt. Lasers Eng.* **2020**, *132*, 106136. [[CrossRef](#)]
6. Nguyen, V.-T.; Kwon, S.-J.; Kwon, O.-H.; Kim, Y.-S. Mechanical Properties Identification of Sheet Metals by 2D-Digital Image Correlation Method. *Procedia Eng.* **2017**, *184*, 381–389. [[CrossRef](#)]
7. Mirone, G.; Barbagallo, R.; Bua, G.; De Caro, D.; Ferrea, M.; Tedesco, M.M. A Simple Procedure for the Post-Necking Stress-Strain Curves of Anisotropic Sheet Metals. *Metals* **2023**, *13*, 1156. [[CrossRef](#)]
8. Sasso, M.; Rossi, M.; Chiappini, G.; Palmieri, G. Sheet Metals Testing with Combined Fringe Projection and Digital Image Correlation. In Proceedings of the SEM Annual Conference, Albuquerque, NM, USA, 1–4 June 2009.
9. Mirone, G.; Corallo, D. Stress–Strain and Ductile Fracture Characterization of an X100 Anisotropic Steel: Experiments and Modelling. *Eng. Fract. Mech.* **2013**, *102*, 118–145. [[CrossRef](#)]
10. Madi, Y.; Garcia, J.-M.; Proudhon, H.; Shinohara, Y.; Helfen, L.; Besson, J.; Morgeneyer, T.F. On the Origin of the Anisotropic Damage of X100 Line Pipe Steel: Part I—In Situ Synchrotron Tomography Experiments. *Integr. Mater. Manuf. Innov.* **2019**, *8*, 570–596. [[CrossRef](#)]
11. Zhu, F.; Bai, P.; Zhang, J.; Lei, D.; He, X. Measurement of True Stress–Strain Curves and Evolution of Plastic Zone of Low Carbon Steel under Uniaxial Tension Using Digital Image Correlation. *Opt. Lasers Eng.* **2015**, *65*, 81–88. [[CrossRef](#)]
12. Zhang, Z.L.; Ødegård, J.; Søvik, O.P.; Thaulow, C. A Study on Determining True Stress–Strain Curve for Anisotropic Materials with Rectangular Tensile Bars. *Int. J. Solids Struct.* **2001**, *38*, 4489–4505. [[CrossRef](#)]
13. Zhang, Z.L.; Hauge, M.; Ošdegard, J.; Thaulow, C. Determining Material True Stress-Strain Curve from Tensile Specimens with Rectangular Cross-Section. *Int. J. Solids Struct.* **1999**, *36*, 3497–3516. [[CrossRef](#)]
14. Cazacu, O.; Rodríguez-Martínez, J.A. Effects of Plastic Anisotropy on Localization in Orthotropic Materials: New Explicit Expressions for the Orientation of Localization Bands in Flat Specimens Subjected to Uniaxial Tension. *J. Mech. Phys. Solids* **2019**, *126*, 272–284. [[CrossRef](#)]
15. Bridgman, P.W. *Studies in Large Plastic Flow and Fracture: With Special Emphasis on the Effects of Hydrostatic Pressure*; Harvard University Press: Cambridge, MA, USA, 1964. [[CrossRef](#)]
16. Mirone, G. Approximate Model of the Necking Behaviour and Application to the Void Growth Prediction. *Int. J. Damage Mech.* **2004**, *13*, 241–261. [[CrossRef](#)]
17. Abedini, A.; Narayanan, A.; Butcher, C. An Investigation into the Characterization of the Hardening Response of Sheet Metals Using Tensile and Shear Tests with Surface Strain Measurement. *Forces Mech.* **2022**, *7*, 100090. [[CrossRef](#)]
18. Marth, S.; Djebien, S.; Kajberg, J.; Häggblad, H.-Å. Stepwise Modelling Method for Post Necking Characterisation of Anisotropic Sheet Metal. *Model. Simul. Mater. Sci. Eng.* **2021**, *29*, 085001. [[CrossRef](#)]
19. Choung, J.M.; Cho, S.R. Study on True Stress Correction from Tensile Tests. *J. Mech. Sci. Technol.* **2008**, *22*, 1039–1051. [[CrossRef](#)]
20. Mirone, G.; Verleysen, P.; Barbagallo, R. Tensile Testing of Metals: Relationship between Macroscopic Engineering Data and Hardening Variables at the Semi-Local Scale. *Int. J. Mech. Sci.* **2019**, *150*, 154–167. [[CrossRef](#)]
21. Habraken, A.M.; Aksen, T.A.; Alves, J.L.; Amaral, R.L.; Betaieb, E.; Chandola, N.; Corallo, L.; Cruz, D.J.; Duchêne, L.; Engel, B.; et al. Analysis of ESAFORM 2021 Cup Drawing Benchmark of an Al Alloy, Critical Factors for Accuracy and Efficiency of FE Simulations. *Int. J. Mater. Form.* **2022**, *15*, 61. [[CrossRef](#)]
22. Corallo, L.; Verleysen, P. On the Anisotropic Mechanical Response of Ti6Al4V Sheet at High Strain Rates. *Key Eng. Mater.* **2022**, *926*, 970–979. [[CrossRef](#)]
23. Tang, B.; Wang, Z.; Guo, N.; Wang, Q.; Liu, P. An Extended Drucker Yield Criterion to Consider Tension–Compression Asymmetry and Anisotropy on Metallic Materials: Modeling and Verification. *Metals* **2019**, *10*, 20. [[CrossRef](#)]
24. Hill, R. A Theory of the Yielding and Plastic Flow of Anisotropic Metals. *Proc. A* **1948**, *1033*, 281–297. [[CrossRef](#)]
25. Hill, R. Constitutive Modelling of Orthotropic Plasticity in Sheet Metals. *J. Mech. Phys. Solids* **1990**, *38*, 405–417. [[CrossRef](#)]
26. Cazacu, O.; Plunkett, B.; Barlat, F. Orthotropic Yield Criterion for Hexagonal Closed Packed Metals. *Int. J. Plast.* **2006**, *22*, 1171–1194. [[CrossRef](#)]
27. Cazacu, O. New Yield Criteria for Isotropic and Textured Metallic Materials. *Int. J. Solids Struct.* **2018**, *139–140*, 200–210. [[CrossRef](#)]

28. Barlat, F.; Lege, D.J.; Brem, J.C. A Six-Component Yield Function for Anisotropic Materials. *Int. J. Plast.* **1991**, *7*, 693–712. [[CrossRef](#)]
29. Barlat, F.; Aretz, H.; Yoon, J.W.; Karabin, M.E.; Brem, J.C.; Dick, R.E. Linear Transformation-Based Anisotropic Yield Functions. *Int. J. Plast.* **2005**, *21*, 1009–1039. [[CrossRef](#)]
30. Mirone, G.; Barbagallo, R.; Tedesco, M.M.; De Caro, D.; Ferrea, M. Mechanical Response of an High-Strength Automotive Steel at Different Strain Rates and Evolution of Damage-Related Parameters. *IOP Conf. Ser. Mater. Sci. Eng.* **2021**, *1038*, 012021. [[CrossRef](#)]

**Disclaimer/Publisher’s Note:** The statements, opinions and data contained in all publications are solely those of the individual author(s) and contributor(s) and not of MDPI and/or the editor(s). MDPI and/or the editor(s) disclaim responsibility for any injury to people or property resulting from any ideas, methods, instructions or products referred to in the content.